PAPER

Effect of water frustration on water oxidation catalysis in the nanoconfined interlayers of layered manganese oxides birnessite and buserite†

Ravneet K. Bhullar,[a] Michael J. Zdilla, [ID] *[a] Michael L. Klein[a] and Richard C. Remsing*[b]

The role of geometric frustration of water molecules in the rate of water oxidation in the nanoconfined interlayer of manganese-oxide layered materials (birnessite, buserite) is examined in a well-controlled experiment. Calcium buserite is prepared, and used in a split-batch synthetic protocol to prepare calcium birnessite, sodium buserite, and sodium birnessite, and partially dehydrated sodium birnessite. Thus, four samples are prepared in which features effecting catalytic efficiency (defect density, average manganese oxidation state) are controlled, and the main difference is the degree of hydration of the interlayer (two layers of water in buserites *vs.* one layer of water in birnessite). Molecular dynamics simulations predict birnessite samples to exhibit geometric water frustration, which facilitates redox catalysis by lowering the Marcus reorganization energy of electron transfer, while buserite samples exhibit traditional intermolecular hydrogen bonding among the two-layer aqueous region, leading to slower catalytic behavior akin to redox reactions in bulk water. Water oxdiation activity is investigated using chemical and electrochemical techniques, demonstrating and quantifying the role of water frustration in enhancing catalysis. Calculation and experiment demonstrate dehydrated sodium birnessite to be most effective, and calcium buserite the least effective, with a difference in electrocatlytic overpotential of ∼750 mV and a ∼20-fold difference in turnover number.

[a]*Department of Chemistry, Temple University, 1901 N. 13th St., Philadelphia, PA 19122, USA. E-mail: mzdilla@temple.edu*

[b]*Department of Chemistry and Chemical Biology, Rutgers University, 123 Bevier Rd., Piscataway, NJ 08854, USA. E-mail: rick.remsing@rutgers.edu*

† Electronic supplementary information (ESI) available: Details on computational methods, ICP-OES data, TOF and TON data, EDS, additional PXRD data, TGA, additional catalysis figures. See DOI: 10.1039/d0ta09635k

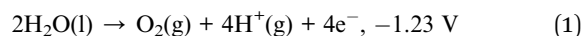## Introduction

Solar hydrogen remains to be realized as a replacement for fossil fuels. Currently, humanity's main source of hydrogen is production from natural gas, which generates carbon dioxide as a byproduct. Hence, a carbon-neutral source of hydrogen does not yet exist, and its use undermines the main incentive of switching to a hydrogen economy: the elimination of fossil fuel consumption.[1] In nature, solar water splitting is achieved by the photosynthetic electron transport chain, with the initial water oxidation step catalyzed by the oxygen evolving complex (OEC), the $CaMn_4$ cluster active site of the photosystem II enzyme of oxygenic photosynthetic organisms. While successful for biology, its use is not facile *in vitro*.[2] The oxygen evolution reaction remains the primary barrier to realization of green hydrogen production by water splitting because of its high activation energy and multi-electron, mechanistically complex

nature. Water splitting is 1.23 V uphill, and the redox half reactions are as follows:

Water oxidation:

$$2H_2O(l) \rightarrow O_2(g) + 4H^+(g) + 4e^-, \; -1.23 \text{ V} \tag{1}$$

Proton reduction:

$$4H^+ + 4e^- \rightarrow 2H_2, \; 0 \text{ V} \tag{2}$$

Traditional benchmarks of water oxidation catalysis are the oxides of Ru and Ir,[3] which operate at low overpotentials of 0.219 V and 0.321 V respectively. However, because of their high cost and limited availability, researchers have been looking for cheaper, eco-friendly, robust and more readily available catalysts for oxygen evolution reaction (OER), with a number of low-overpotential materials having been discovered in the past decade made from more abundant elements. These include a number of classes of layered materials such as manganese oxides,[4] cobalt oxides,[5] nickel oxides,[6,7] and double-layer hydroxides.[8,9]

Birnessite and buserite are layered manganese oxides of particular interest. Both birnessite and buserite are important manganese containing phases forming a major component of deep-sea nodules and desert varnish. Because of their chemical and topological analogy with the catalytically active site of

photosystem II, low cost, high abundance and green cleaning, extensive studies have been conducted on birnessites to assess and enhance their catalytic activity towards water splitting.[10,11] Birnessite comprises two-dimensional, atomically thin layered, anionic MnO_2 sheets with mixed Mn(III)/Mn(IV) and average oxidation state ranging between 3.51–3.80, separated by 7.25 Å and containing a monolayer of Lewis cations and water molecules in the interlayer region (Fig. 1).

While birnessite was traditionally regarded as a poor water oxidation catalyst, with overpotentials typically in the range of 800 mV, recent work has demonstrated the enhancement of water oxidation activity beyond that of even the best Mn–O based water oxidation catalysts. This may be achieved by selection of interlayer cations,[11] enrichment of Mn(III) defects,[3] intercalation of interlayer transition metal ions,[12] in-layer cobalt doping of birnessite nanosheets,[13] periodic distribution of Mn(III) in adjacent layers,[14] by the enhancement of geometric frustration of water molecules in the interlayer region[11] and by a combination of these approaches.[15] Buserite is identical to birnessite except for a greater interlayer separation of 10 Å, which accommodates a double layer of water and cations instead of birnessite's single layer (Fig. 1).

Theoretical and molecular modeling studies based on interstitial hydration structure of birnessites have been previously explored by our group.[11] The frustrated hydration structures in the crowded birnessite interlayer can lead to an enhanced electron transfer rate in the oxidation step of water splitting and hence enhance catalytic activity for water oxidation. This is because the supersaturation of this interlayer by the interstitial cations prevents the complete coordination of these cations by water molecules, leading to enhanced fluctuations, which reduces the reorganization energy (λ) in the Marcus description of electron transfer. While we have examined this phenomenon in a detailed report of molecular dynamics simulation supported by vibrational spectroscopy,[11] and exploited the phenomenon in several reports where we use this frustrated interlayer environment to enhance catalytic activity by nickel and cobalt ions, these studies were complicated by the simultaneous alteration of more than one feature of these birnessites in our comparative samples. For example, by the introduction of in-layer[16] or interlayer transition metal ions,[12] we altered not only the degree of water frustration, but also the Mn(III) content, defect density, in-layer hole mobility and interlayer conductivity. In this report, we provide a controlled experiment to test the role of water frustration by catalytic assessment of analogous birnessite and buserite samples from the same split-batch synthetic material so that comparable birnessite and buserite samples may be evaluated that have similar average manganese oxidation state, the same interlayer cation content, the same defect density and where the only major difference is that of the interlayer water structure. We have examined two sets (interlayer Na^+ *vs.* Ca^{2+}) of buserite and birnessite samples, as well as partially dehydrated birnessite with an even greater degree of expected water frustration. These experiments permit a well-controlled evaluation of the role of water frustration apart from influences of other properties of synthetic layered manganese oxide samples.

Materials and methods

General considerations

All reagents were purchased from chemical vendors and used without further purification. X-ray diffraction (XRD) was performed on Bruker APEXII DUO diffractometer using Mo Kα radiation from a sealed tube and processed using the DIF-FRACEVA software package. Patterns were indexed to the Crystallography Open Database (COD). The five compounds presented in this work were each indexed to the following COD ID#: Na-buserite: 9013650, Na-birnessite: 9013651, Ca-buserite: 9010155, Ca-birnessite: 9013652, dehydrated birnessite: 9002843. Indexed unit cells were refined using Rietveld refinement. Transmission electron microscopy (TEM) images were collected using a JEOL JEM-1400 microscope operating at 120 kV. Scanning electron microscopy and energy dispersive spectroscopy (SEM-EDS) samples were deposited on conductive carbon tape mounted on aluminum stubs and images were collected on an Agilent 8500 FE-SEM instrument operating at 1 kV. All manganese oxide samples were analyzed for elemental content using SEM-EDS and Inductively coupled plasma optical emission spectroscopy (ICP-OES) using a Thermo Scientific iCAP 7000 Series ICP-OES instrument. IR spectroscopy data was collected using a Thermo Scientific iS5 spectrometer with an iD5 ATR attachment. LSV data was collected using CHI 660E electrochemical instrument using glassy-carbon working electrode, 1 M KOH as electrolyte solution, Pt wire as counter and saturated calomel as reference electrode.
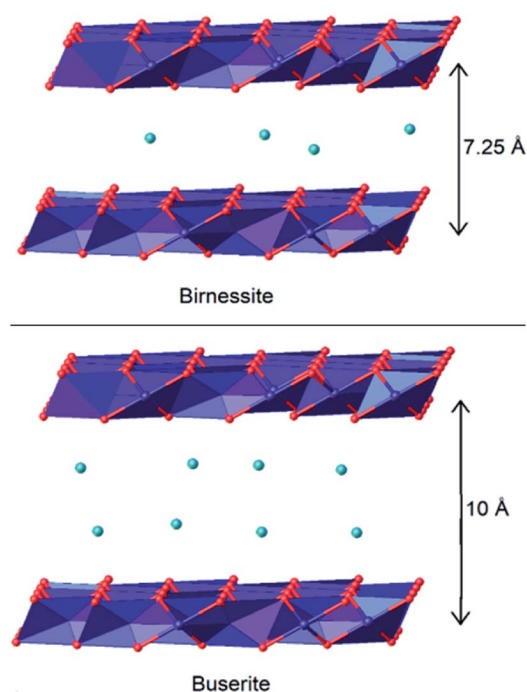

Fig. 1 Structures of birnessite and buserite. Each is a layered oxide of octahedral manganese(III/IV) with hydrated interlayer cations. Birnessite has a single layer of cations and a smaller 7.25 Å spacing while buserite has two layers of hydrated interstitial cations and a larger 10 Å spacing.

This journal is © The Royal Society of Chemistry 2021

J. Mater. Chem. A, 2021, **9**, 6924–6932 | **6925**

Computational methods

To characterize the structure in the birnessite and buserite interlayers, we performed molecular dynamics (MD) simulations following the protocol used in previous work.[11] Simulations were carried out using the GROMACS5 (ref. 17) software package and the CLAYFF[18] force field to describe interatomic interactions, modified to include Mn.[19] The MnO_2 sheets are held fixed in their equilibrium structure, and we leave the edges of birnesite and buserite open to water reservoirs in order to allow chemical exchange between interlayers. The simulated dehydrated birnessite, birnessite, and buserite systems have interlayer spacings of 5.65 Å, 7.52 Å, and 10.42 Å, respectively.

Synthesis of Na-buserite

Solutions of 12.589 g (0.064 mol) of $MnCl_2$ and 80.67 g (2.017 mol) of NaOH each in 250 mL of deionized water were prepared. These solutions were kept in an ice bath and sparged with N_2 gas for 1 hour. The $MnCl_2$ solution was slowly added to NaOH solution with continued N_2 sparging in an oil bath at room temperature. The solution changed to a brown suspension. The N_2 purging was replaced with O_2 bubbling for 5 hours forming dark brown precipitate. The suspension was heated to 80 °C and aged for 9 hours. The flask was cooled to room temperature and the solid isolated by filtration, and the identity of buserite was confirmed by PXRD (Fig. 3). Before it was permitted to dry, the suspension was immediately split into two batches for subsequent syntheses as described below.[20,21]

Stabilization of Na-buserite and preparation of Na-birnessite

The dark brown precipitate from the above synthesis of Na-buserite was washed with deionized water till the pH of the solution was below 9.5. About 3/4 of the wet product was transferred to a beaker and suspended in 1000 mL of deionized water and stirred for 48 hours. The product was stored underwater to preserve the buserite structure from dehydrative decomposition into birnessite.[4] Unit cell: triclinic C, $a = 5.1342$ Å, $b = 2.8469$ Å, $c = 10.200$ Å, $\alpha = 90.31°$, $\beta = 101.559°$, $\gamma = 89.944°$. The remaining 1/4 of the product was air-dried, which resulted in spontaneous conversion into 12.5 g of Na-birnessite based upon PXRD (Fig. 3). Unit cell: triclinic C, $a = 5.1298$ Å, $b = 2.8445$ Å, $c = 7.2129$ Å, $\alpha = 90.12°$, $\beta = 101.395°$, $\gamma = 89.958°$.

Synthesis of Ca-buserite

A 500 mL solution of 1 M $CaCl_2$ was prepared and treated with 5 mL of Na-buserite suspension (resuspended by gentle shaking) and stirred for 48 hours to facilitate ion exchange.[22,23] The product was filtered and air dried overnight to give 5.0 g of Ca-buserite based on PXRD (Fig. 3). Unit cell: triclinic C, $a = 5.178$ Å, $b = 2.8509$ Å, $c = 10.200$ Å, $\alpha = 89.45°$, $\beta = 103.18°$, $\gamma = 89.91°$.

Synthesis of Ca-birnessite

2 g of Ca-buserite was heated at 60 °C for 24 hours producing 1.75 g of Ca-birnessite based on PXRD (Fig. 3).[24] Unit cell: triclinic C, $a = 5.1349$ Å, $b = 2.8465$ Å, $c = 7.251$ Å, $\alpha = 89.94°$, $\beta = 101.561°$, $\gamma = 89.997°$.

Synthesis of partially dehydrated birnessite

2 g of Na-birnessite was heated to 300 °C at the rate of 1 °C per minute in an oven for 4 hours, cooled to room temperature, and was indexed using PXRD. Unit cell: triclinic P, $a = 2.9513$ Å, $b = 2.9547$ Å, $c = 5.651$ Å, $\alpha = 78.72°$, $\beta = 101.79°$, $\gamma = 122.33°$. The thermogravimetric analysis (Fig. S4†) revealed 15.3% of mass loss of water as a result of heating the birnessite sample to 300 °C for 4 hours. Partially dehydrated birnessite was tested for its reversible conversion back to standard birnessite by treating 50 mg of the sample with water for 72 hours. The PXRD pattern (Fig. S3†) shows that the conversion of dehydrated birnessite to standard hydrated birnessite is complete and hence the dehydration is reversible. Heating beyond 300 °C (Fig. S5†) results in decomposition, due to the collapse of the lattice upon the loss of all water, and was thus avoided.

Oxygen evolution reaction (OER) catalysis

The efficiency of these materials towards chemical water oxidation was tested using ceric ammonium nitrate as a chemical oxidant (0.04 M, 5 mL) and monitored with a Hach HQ30d portable meter kit with LDO101 optical dissolved oxygen probe. A suspension of about 30 mg of the catalyst in 20 mL of degassed water (prepared by bubbling Ar gas for atleast 3 hours) was prepared and sonicated for 5 minutes to ensure homogeneous suspension of the sample. An N_2 blanket was applied to the suspension along with O_2 probe as previously described.[3] The 5 mL of ceric ion solution was then injected to the catalyst suspension and O_2 evolution was measured over time (pH ≈ 2). The O_2 yield was normalized by total Mn molar content, as determined by ICP-OES (Table S1†) to give O_2 yield in units of mmol of O_2/mg of Mn.[25]

Electrochemical surface area (ECSA)

For each sample the electrochemical surface area was determined by the comparison of double-layer capacitance measured by cyclic voltammetry to an ideal electrode.[26] The catalyst ink was prepared by dissolving 4 mg of catalyst, 4 mg of carbon dispersed in 1 mL of isopropyl alcohol and 35 μL of Nafion solution (5% in alcohol, Ion Power Inc.). The mixture was sonicated for 1 hour to suspend the particles homogeneously.[16] The catalyst ink was drop cast on glassy carbon electrode with a loading of 0.28 mg cm^{-2}. Coating thickness was between 241 and 254 μm as measured by optical microscopy. Cyclic voltammograms were obtained at variable scan rates between 0.001 and 0.01 V s^{-1} and the resulting difference between anodic and cathodic current was compared to that for a polished 7.1 mm^2 glassy carbon electrode for determination of equivalent catalytic surface area. See ESI† (Section 9) for data.

Linear sweep voltammetry

Tests for OER activity were performed at a sweep rate of 10 mV s^{-1} at a pH of 14 (1 M KOH solution). All the potentials were
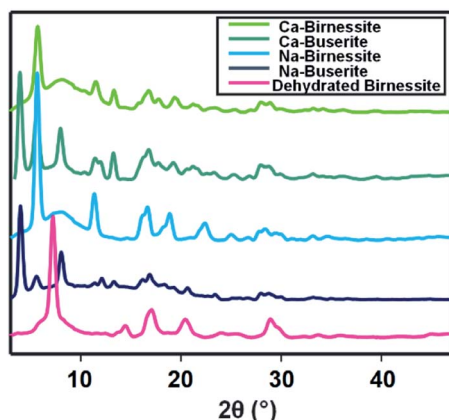
6926 | J. Mater. Chem. A, 2021, 9, 6924–6932

This journal is © The Royal Society of Chemistry 2021

Fig. 2 XRD patterns of standard triclinic birnessite, buserite and dehydrated birnessite samples.

Fig. 4 TEM images. (A) Ca birnessite, (B) Ca buserite, (C) Na birnessite, (D) Na buserite, (E) dehydrated birnessite.

measured with respect to a standard calomel reference electrode (CH instruments) and Pt wire was used as the counter electrode, and corrected to NHE. The catalyst ink was prepared as described above (ECSA section). All the catalysis trials were run in triplicate.

Results

Characterization

The PXRD pattern (Fig. 2) of Ca-buserite showed (001) peak at a d-spacing of 10.20 Å (3.99° 2θ), corresponding to the stacking distances in the vertical direction (see Fig. 1). However, after converting to Ca-birnessite, the (001) peak shifted to 7.25 Å (5.62° 2θ) due to loss of interlayer water molecules. A similar trend was observed after converting Na-buserite to Na-birnessite, (001) peak shifted from 10.20 Å to 7.21 Å (3.99° and 5.64° 2θ) respectively. The (001) peak after partial dehydration shifted from 7.21 Å to 5.65 Å (5.64° and 7.76° 2θ) which is typical of dehydrated birnessite.[27]

SEM images (Fig. 3) suggest that the flower-pod morphology typical of birnessite and buserite was maintained regardless of the addition or removal of interlayer water molecules. TEM images (Fig. 4) show a similar layered structure for all the samples.

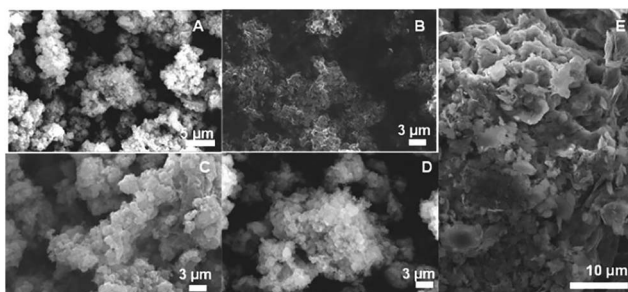FTIR spectra of birnessite and buserite samples are shown in Fig. 5. The absorption peaks around 3200 cm^{-1} correspond to the OH-stretch of water molecules. The bending vibration peaks of interlayer water molecules were observed around 1600 cm^{-1}. However, these peaks were broader in buserite samples as compared to birnessites, which indicates a greater degree of hydrogen-bonding between interlayer water molecules in buserite due to a larger distribution of dielectric environments in hydrogen-bonded water. The peaks around 600 cm^{-1} are characteristic of Mn–O stretch in birnessite.[27]

Electrochemical surface area measurements on catalytic materials were determined using electrochemical measurement of double-layer capacitance. These measurements on buserite, birnessite, and dehydrated birnessite can offer insights into whether changes in catalytic activity could merely be a function of surface area. These measurements show that upon conversion of buserite to birnessite by dehydration and collapse of the stacking distance, the electrochemically active surface area decreases by about half. Dehydration of sodium birnessite by further heating did not change the electrochemically active surface area. These data are presented in Table S6 and Fig. S8–S12.†

High-resolution X-ray photoelectron spectra were obtained for each sample and fit for the approximation of average oxidation state using the approach of Nesbitt.[28] Average

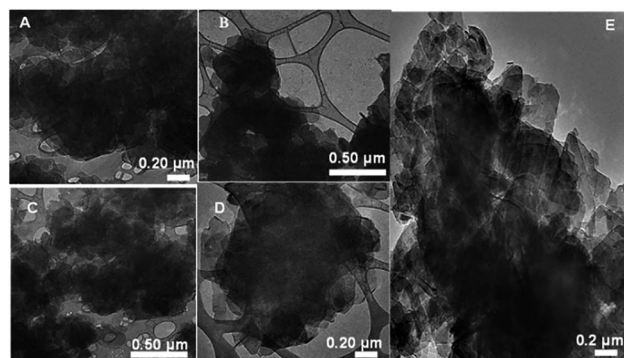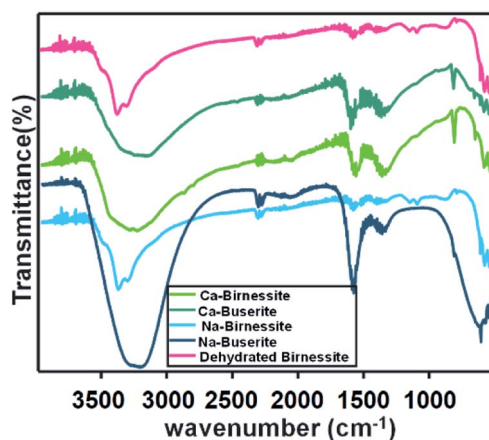Fig. 3 SEM images. (A) Ca birnessite, (B) Ca buserite, (C) Na birnessite, (D) Na buserite, (E) dehydrated birnessite.

Fig. 5 FTIR spectra of birnessite and buserite samples.

This journal is © The Royal Society of Chemistry 2021

J. Mater. Chem. A, 2021, 9, 6924–6932 | 6927

oxidation states (AOS) were similar for the samples. AOS 3.52 for Ca-birnessite, 3.64 for Na-birnessite, and 3.55 for dehydrated Na-birnessite. XPS of Na-busserite could not be determined due to dehydration of the material under vacuum back to birnessite. XPS of calcium buserite gave a slightly higher AOS of 3.72. XPS spectra are provided in the ESI.†

Catalytic activity. OER activity was tested by using glassy carbon electrode with a deposited catalyst ink in electrochemical experiments. Chemical catalytic activity was tested by exposing the catalyst to the chemical oxidant (ceric ammonium nitrate) which can drive water oxidation in the presence of a catalyst.

$$2H_2O + 4Ce^{4+} \rightarrow O_2 + 4Ce^{3+} + 4H^+ \qquad (3)$$

The results of these experiments are illustrated in Fig. 6. The electrochemical activity of layered phases improved with
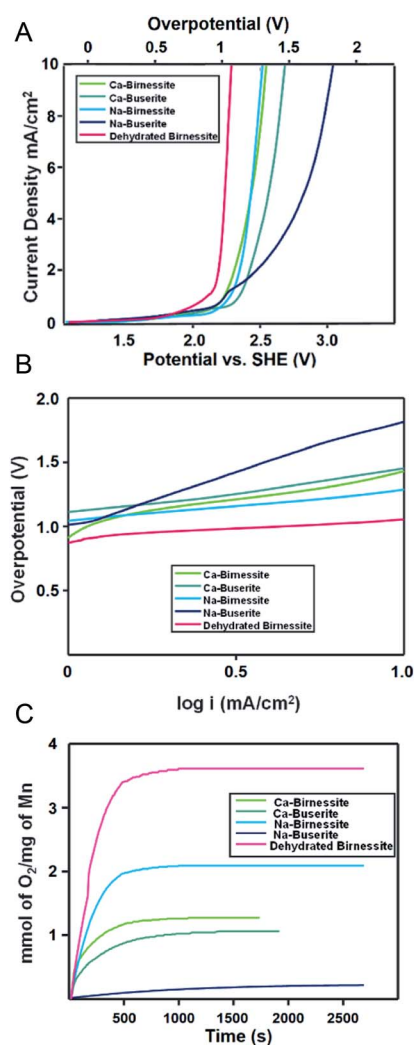

Fig. 6 OER activity of the catalysts. Top: linear sweep voltammetry (10 mV s^{-1}); standard calomel reference electrode and Pt wire was used as the counter electrode. Center: Tafel plot. Bottom: oxidation of water by ceric ion catalyzed by birnessite and buserites with mmol of O$_2$ evolved normalized by mass (mg) of Mn.

decreasing interlayer water content. The overpotential decreased from 1.815 V in Na-buserite to 1.286 V in Na-birnessite. Similarly, the overpotential decreased from 1.455 V in Ca-buserite to 1.297 V in Ca-birnessite. After the further removal of water molecules in the interlayer, the overpotential decreased to 1.056 V in dehydrated Na-birnessite (Fig. 6A). The Tafel plot improved from The Tafel plot improved from 900.5 mV dec^{-1} in Na-buserite to 212.2 mV dec^{-1} in Na-birnessite and 113.2 mV dec^{-1} in dehydrated Na-birnessite (Fig. 6B).

The chemical oxidation in the presence of ceric ammonium nitrate showed similar trends (Fig. 6C). The standard Na-birnessite was active for approximately 45 minutes. Increased OER rate was observed with diminishing interlayer water molecules (Table S2†). Dehydrated birnessite possessed highest activity with a turn over number (TON) of 198 mmol of O$_2$/mol of Mn, in comparison to Na-birnessite with a TON of 114 mmol of O$_2$/mol of Mn and Na-buserite with a TON of 11 mmol of O$_2$/mol of Mn. The TON increased from 56 mmol of O$_2$/mol of Mn in Ca-buserite to 68 mmol of O$_2$/mol of Mn in Ca-birnessite. The standard deviation plots for the oxygen evolution reaction run in triplicate have been described in Fig. S6.†

The broadening of peaks in the PXRD patterns (Fig. S2†) of the samples post catalysis indicated that the catalysts undergo structural damage during water oxidation, which could be because of the introduction of ceric ions in the interlayer region[3] or oxidative damage to the sheet structure. The interlayer region of dehydrated birnessite was observed to be hydrated during the water oxidation catalysis because of the shift of (001) peak to 7.25 Å in the post-catalysis PXRD pattern (Fig. S2†), which may participate in its eventual failure.

Discussion

Due to a high degree of variability in the activities, surface areas, average oxidation state, and defect density of synthetic layered manganese oxides, examination of the role of a single phenomenon on catalysis is difficult, since different batches of layered MnO$_2$ will have variation in several correlated properties. In order to test the role of water frustration on catalytic efficiency, a controlled preparation of partially dehydrated birnessite, regular birnessite, and buserite samples was performed with structural and compositional control in mind. To achieve this, we prepared a series of layered manganese oxides using variations on a protocol for triclinic birnessite. While this polymorph of birnessite is less active in catalysis than the hexagonal birnessite used in our previous studies,[3] it is advantageous for this controlled experiment as it has relatively lower defect density and higher crystallinity. To prepare this series, a split batch method was used whereby individual samples of sodium birnessite are split and converted to sodium buserite, calcium buserite, calcium birnessite and partially dehydrated birnessite under mild conditions. By this approach, the structure and composition of the anionic MnO$_2$ sheets is maintained across samples to the maximum degree possible, and the only significant difference between samples is the interlayer content, *i.e.*, cation identity and degree of hydration. Characterization of

6928 | *J. Mater. Chem. A*, 2021, **9**, 6924–6932

This journal is © The Royal Society of Chemistry 2021

the samples by XRD confirms the expected interlayer spacing of birnessite and buserite samples by the difference in the position of the 001 and 002 Bragg peaks of buserite (3.99° and 5.62° respectively) in comparison to birnessite (5.64° and 11.2°, Fig. 2). This corresponds to a difference in interlayer spacing: 7.25 Å and 10.20 Å for birnessite and buserite respectively, due to difference in the number of cation/water layers. The presence of a second water layer in buserite "dilutes" the interlayer concentration of the cations and is expected to result in a greater degree of inter-water hydrogen bonding. FTIR shows an increase in broadness of the O–H stretch (3200 cm^{-1}) and bend (1600 cm^{-1}) resulting from increased hydrogen bonding among water molecules, which widens the range of stretching frequencies due to a large array of dielectric environments of the O–H bonds. While the difference between the Na-birnessite and buserite OH peak widths in Fig. 6 is clear, the peak width difference for the Ca-containing samples is more subtle in the case of the OH stretching peak (3200 cm^{-1}), and not apparent at all for the OH bending mode (1600 cm^{-1}). This is most likely due to decreased water frustration in Ca-birnessite than in K-birnessite; the higher charge of the Ca^{2+} requires half the concentration in comparison to K$^+$ ions in order to achieve charge balance. The lower concentration of Ca^{2+} ions suggests a greater opportunity for H-bonding in interlayer water molecules in Ca-birnessite, leading to broader OH stretches in Ca-birnessite than in K-birnessite.

The samples were tested for their catalytic efficiency for water oxidation/oxygen evolution reaction based upon two approaches: electrochemical oxygen evolution reaction under alkaline conditions, and chemical water oxidation/oxygen evolution reaction by ceric ion under acidic conditions (~pH = 2). It is worthwhile to note that these samples do not represent excellent catalysts like those we have reported previously.[3] This is because the purpose of this report is not to maximize catalytic efficiency, but to test the role of a single phenomenon: water frustration. Therefore, in this report we deliberately avoid catalytic enhancement by other means available, including Mn(III) enrichment, structural defect incorporation and dopants, which improve the catalytic activity. Instead, we focus here on a well-controlled comparison using a synthetic approach[14,21] that minimizes defects so that the role of interlayer hydration may be directly assessed apart from other influences. Independent of whether chemical or electrochemical oxidation is examined, a general trend emerges that as the level of interlayer hydration decreases from buserite to birnessite to dehydrated birnessite, the catalytic efficiency towards water oxidation increases. The latter result is consistent with a previous report from Chen et al. that demonstrated that annealing of a nickel birnessite OER catalyst resulted in a decrease in interlayer spacing, and corresponding increase in catalytic activity.[29] In this report, a change in Mn oxidation state from annealing, and a change in charge transfer resistance was cited as a cause for the increase in catalytic activity. As our oxidation state also decreases slightly (0.1 e$^-$ per manganese) upon formation of dehydrated birnessite at 300 °C, this effect could also be in play for dehydrated birnessite. However, this oxidation state change is small, and likely within experimental

error of the XPS fitting. Further, high-temperature annealing is was not undertaken for buserite-birnessite conversion reactions, and probably does not drive significant redox chemistry. Further, it is worthwhile to note that the electrochemically active surface area (ESI†) decreases by about half upon the conversion of buserite to birnessite, and does not change significantly upon dehydration of birnessite. Therefore, active surface are does not explain the difference in catalytic activity.

At first the observation that decreasing interlayer hydration improves catalysis might seem counterintuitive since water is the catalytic substrate, and since normally, reaction rates are presumed proportional to (some power of) the concentration of the substrate. Our past work predicted[11] that geometric frustration of interlayer water increases relevant fluctuations of water, leading to faster redox catalysis based on Marcus theory, even though there is less water present. We have exploited this prediction to generate some of the most active Mn-based water oxidation catalysts known,[3,11–14,20] but until now have yet to offer a well-controlled examination of the role of this water frustration in the absence of other rate-enhancing effects.

While XRD analysis provides an understanding of the structure of the MnO$_2$ sheets of layered manganese oxides, in order to understand the role water frustration plays on enhancing catalysis in layered manganese oxides, a molecular-scale view is required. Spectroscopic investigation and molecular dynamics simulations provide these insights. Birnessite and buserite have Lewis cations in the interlayer region which are surrounded by water molecules forming a hydration
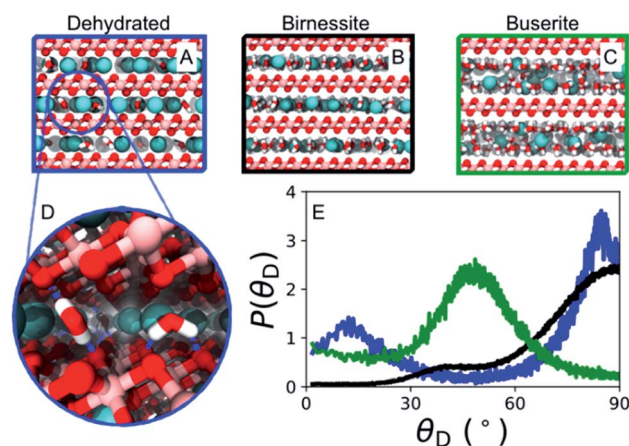

Fig. 7 Simulated models of (A) dehydrated birnessite, (B) birnessite, and (C) buserite, illustrating the single layer of water ions in birnessite and double layer in buserite. Also shown in (D) is a zoomed in snapshot of representative orientations of water molecules in the dehydrated birnessite system with the angle made by the water dipole moment vector and the MnO$_2$ surface normal (θ_D) ≈ 90° (left water) and θ_D ≈ 15° (right water). (E) The probability distribution for θ_D, $P(\theta_D)$, for (blue) dehydrated birnessite, (black) birnessite, and (green) buserite. The structure of interlayer water changes significantly upon moving from buserite to birnessite. Upon partial dehydration of birnessite, the overall distribution is similar, but the peak at 40° disappears and a peak at low θ_D emerges that is consistent with water molecules donating two hydrogen bonds to one surface, i.e. the rightmost water in panel (D).

This journal is © The Royal Society of Chemistry 2021

J. Mater. Chem. A, 2021, **9**, 6924–6932 | **6929**

structure; see Fig. 7A–C for an illustration. In buserite, the interlayer cations are expected to be better hydrated because of the presence of two layers of water molecules, but no extra cations (the number of cations is defined by the average oxidation state in the MnO sheets). Indeed, our MD simulations predict that the coordination number of K^+, (including ions at the solvent exposed interlayer edges), increases according to the following series: 1.5, 4.8, 7.8 water molecules per K^+ upon increasing the interlayer distance from dehydrated birnessite to birnessite to buserite respectively. The number of water–water hydrogen bonds also increases, resulting in more bulk-like water in buserite. This is consistent with the observed broadened water O–H stretch signals at 3200 cm^{-1} in the IR spectrum of buserite in comparison to birnessite (Fig. 5). This is especially germane to the case of the Na-birnessite samples, which have a larger ion concentration due to the lower charge on Na^+ compared to Ca^{2+}. This results in more cations required to balance the negative charge on the sheets, and therefore greater Na^+ concentration and more frustrated water molecules than expected for Ca^{2+} (Fig. 5). Because of the bulk-like ordering of water molecules in buserite, there is a large reorganization energy associated with electron transfer, and consequently electron transfer rates at these hydrated ions are slow (*e.g.* 30 ms^{-1} for aqueous redox ions in direct contact).[30,31] Of the three classes of materials we examine here, buserite is the most bulk-water-like, having well-hydrated cations and a significant degree of inter-water hydrogen bonding.

The geometric constraints and orientational tendencies of water in the three sample types are illustrated by the molecular dynamics simulations. In birnessite, water molecules predominantly orient their dipoles perpendicular to the MnO_2 surface normal ($\theta_D \approx 90°$, Fig. 7E, black data). A small fraction of water molecules form water–water hydrogen bonds, orienting their dipoles at $\theta_D \approx 40–50°$. We have previously argued from MD that the perpendicularly oriented $\theta_D \approx 90°$ water molecules are geometrically frustrated, giving rise to enhanced polarization fluctuations and enhanced electron transfer rates. This behavior is illustrated in a previously published ESI Movie.†[11] The intermolecular water–water hydrogen bonded molecules at $\theta_D \approx 40–50°$ are not frustrated, and do not contribute much to the enhancement of electron transfer rates.[11] Upon dehydration, birnessite experiences an increase in the proportion of perpendicularly aligned water molecules, and the intermolecular water–water hydrogen bonding peak disappears. A new, small peak at $\theta_D = 15°$ appears, corresponding to water molecules doubly hydrogen bonded to oxide ions of the same MnO_2 sheet (Fig. 7D and E, blue data). The dynamics of this model system are visualized in the ESI Movie.†

In contrast, in buserite, water molecules hydrogen bond in a fashion similar to bulk water, and almost all of them orient their dipoles toward interlayer cations at an angle θ_D of about 40–50°, as illustrated in the histogram in Fig. 7E. Unlike birnessite and dehydrated birnessite, there are no water molecules hydrogen bonded across the sheets and aligned perpendicularly (Fig. 7E, green data).

To gain a qualitative understanding of electron transfer in these materials, we can consider redox reactions in the confined interlayer space within a Marcus theory framework. In this context, there are two fundamental quantities: the transfer coefficient, which is proportional to wavefunction overlap between the two species involved in electron transfer, and the solvent reorganization energy. The amount of overlap increases as the distance between the donor and acceptor decrease. Thus, decreasing the distance between Mn and other redox active species (ions and other MnO_2 sheets) serves to increase this component of the electron transfer rate. Indeed, upon partially dehydration of birnessite, the Mn-interlayer-ion distance decreases from 4.3 Å to 2.8 Å, and is expected to increase overlap (electronic communication) and the rate of electron transfer between the sheet and a redox-active interlayer ion.

The reorganization energy determines the free energy barrier for electron transfer. This originates from the free energetic cost for the solvent to reorganize to a minimum energy configuration in response to a polarization state that makes the donor and acceptor equivalent with respect to the electron. Without a change in the chemistry of the system, the reorganization energy decreases as the interlayer ion coordination number decreases, because there are fewer solvent molecules that must reorganize. Thus, a qualitative perspective based on Marcus theory suggests that decreasing the interlayer spacing will lead to an increase in electron transfer rates. However, the birnessite system presents additional mechanisms for the reorganization energy to decrease even beyond this qualitative picture.

Previous work has shown that electron transfer rates are increased beyond Marcus theory expectations due to frustrated solvation of interlayer ions.[11] Water molecules in birnessite are geometrically frustrated because there are too few of them to satisfy the coordination sphere of the interlayer countercation, in combination with their orientation (Fig. 8). As such, this frustration enhances fluctuations of water molecules in birnessite trying to seek a stable configuration. This enhancement of fluctuations makes it easier (thermodynamically) for water to reorganize in a manner conducive to electron transfer (even electron transfers that don't involve the interlayer cations), which in turn lowers reorganization energies, and is thus predicted to further enhance electron transfer rates.

Geometric frustration in birnessite arises from water molecules that H-bond to both MnO_2 sheets and orient their dipole moment perpendicular to the MnO_2 normal. Such structures dominate in both regular and dehydrated birnessite, though in dehydrated birnessite, there is no persistent internal water H-bonding at all, and another minority orientation is observed in the simulation as well, with a water molecule doubly hydrogen bonded to the same MnO_2 sheet ($\theta_D = 15°$, Fig. 7D and E). This additional orientational degree of freedom provides another source of frustration because "up" and "down" orientations are equivalent, leading to more degrees of freedom and further enhancement of dynamical behavior. In this sense, water in dehydrated birnessite is frustrated in three-dimensions (3D), while water in birnessite is frustrated in two-dimensions (2D), and water in buserite is unfrustrated. One may then expect that the increased frustration in dehydrated birnessite will enhance water polarization fluctuations relevant
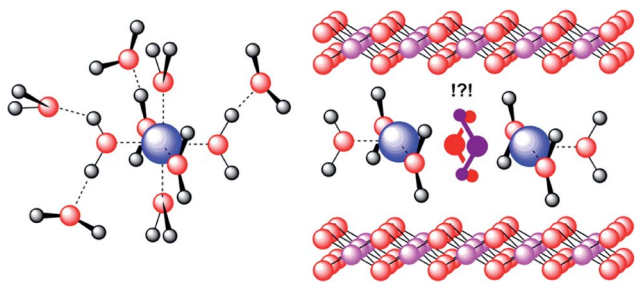
6930 | *J. Mater. Chem. A*, 2021, **9**, 6924–6932

This journal is © The Royal Society of Chemistry 2021

Fig. 8 Illustration of the phenomenon of interlayer frustrated solvent water. Left: bulk solvated ion with water–water hydrogen bonding and no geometric frustration. Right: nanoconfined, water-solvated ions in an interlayer. The central water experiences geometric frustration due to insufficient solvent for complete solvation of ions, leading to enhanced water fluctuations.

Fig. 9 Free energy, $\beta \Delta F(\Delta \tilde{E}) = -\ln P(\Delta \tilde{E})$, as a function of the reduced energy gap, $\Delta \tilde{E} = \Delta E / \Delta s J_{XY}$, for the charge frustrated XY model (CFXY) and the modified CFXY model (mCFXY), shown as data points (see ESI for model details†). The solid curves indicate the corresponding parabolic free energy surfaces obtained by fitting the left side of the computed free energy. The light gray curve is a representative parabolic estimate of the free energy surface for the product state, illustrating how the free energy barrier (intersection with data points) changes with frustration. Note that electron transfer in buserite is expected to follow Marcus theory, *i.e.* the solid blue parabola, but with larger reorganization energies due to the larger coordination number of ionic hydration shells, with respect to birnessite.

to electron transfer beyond those occurring in birnessite, and consequently enhancing electron transfer rates.

The effects of water frustration on electron transfer were previously explained by developing and analyzing a lattice model that exhibits a competition between dipole alignment and ion solvation, the charge frustrated XY (CFXY) model.[11] This competition leads to frustration in a solution containing only cations, as is the case for the systems studied here. To illustrate that the emergence of out-of-plane water orientations increases frustration—by moving from 2D to 3D frustration—we extend the CFXY model to include a description of the out-of-plane degrees of freedom. In brief, we introduce an additional variable, z_i, for solvent degrees of freedom that is equal to 0 if the solvent molecule dipole is parallel to the MnO_2 sheet, +1 if it is pointing out-of-plane "upward," and −1 if it is pointing out-of-plane "downward." When a molecule is pointing out-of-plane, its interactions with other solvent molecules and ions are reduced, consistent with the change in the orientation of water dipoles. The model is described in detail in the ESI.†

Using this modified CFXY model (mCFXY), we carried out the same calculations as in ref. 11; we mimic electron transfer by changing the charge on a single ion and monitoring the energy gap order parameter, ΔE, which adequately describes the progress of a hypothetical electron transfer reaction between interlayer ions and the MnO_2 sheets. The free energy as a function of the energy gap, $\beta \Delta F(\tilde{E}) = -\ln P(\tilde{E})$, is shown in Fig. 9 for the CFXY model with the z_i modification (mCFXY) and without out-of-plane orientations (CFXY), both in the reactant basin where frustration-enhanced fluctuations are most relevant. The free energy basin for the 3D frustrated system is wider, indicating a lower reorganization energy for the electron transfer reaction. Moreover, the deviations of $\Delta F(\Delta E)$ from the parabolic form predicted by Marcus theory (solid lines) is also more significant for the modified (mCFXY) model. This deviation is an immediate consequence of frustration, and the increased deviation in the modified CFXY model is consistent with its increased number of frustrated degrees of freedom compared to the CFXY. We also show a representative Marcus parabola for the product state in the normal regime to illustrate that the barrier for electron transfer (crossing point between
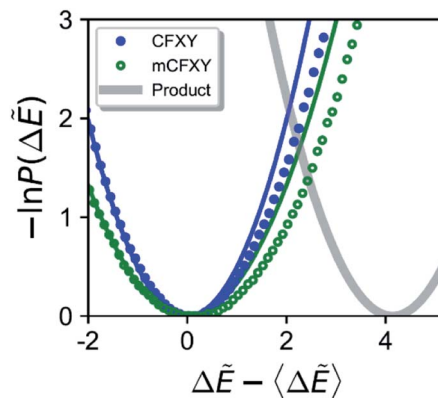
parabolas) is reduced upon the inclusion of out-of-plane solvent orientation. That is, the electron transfer rate is increased when increasing the frustration of solvent molecules from 2D to 3D, as illustrated by birnessite (2D) and dehydrated birnessite (3D) simulations. Because buserite does not exhibit frustration, its corresponding free energies will not exhibit significant deviations from the Marcus parabolas. This alone will lead to lower electron transfer rates. As discussed above, the increased number of coordinating water molecules around each ion will further increase the reorganization energy, narrowing the parabolic free energy surfaces and further reducing electron transfer rates of buserite with respect to birnessite.

Conclusions

The nanoconfined interlayer of layered materials can enhance redox catalysis by the nature of the frustrated solvent molecules therein, which lower the reorganization energy for electron transfer and increase catalytic efficiency. This has been shown to result in remarkable increases in catalytic activity of simple ions when placed into the birnessite interlayer. However, up until now, there has been no conclusive controlled experiment to parse the role of solvent frustration from other factors (defect density, conductivity, average oxidation state, band structure) that could enhance catalysis in in-layer doped layered materials. We demonstrate here that layered materials constructed from the same batch of nanosheet, but with differing interlayer structure exhibit significant differences in catalytic activity for chemical and electrochemical water oxidation. The dominant factor in these differences is the enhancement of relevant water fluctuations due to geometric frustration. Although frustration

This journal is © The Royal Society of Chemistry 2021

J. Mater. Chem. A, 2021, **9**, 6924–6932 | **6931**

can enhance orientational, dielectric polarization fluctuations, the high level of confinement in birnessite can significantly hinder translational motion.[32] The slow translational motion results from the formation of hydrogen bonds between water and the two confining MnO_2 sheets, which need to be broken in order for water to diffuse. Despite this slow diffusion, the slow migration of reactants and products throughout the interlayer is less important for catalytic efficiency than electron transfer rates, as evidenced by the higher activity of birnessite over buserite. We expect that future work examining the mechanisms of translational and rotational diffusion within the birnessite interlayer will aid in further understanding and engineering the catalytic properties of these materials.

Conflicts of interest

There are no conflicts to declare.

Acknowledgements

Notes and references

1 T. Bak, J. Nowotny, M. Rekas and C. C. Sorrell, *Int. J. Hydrogen Energy*, 2002, **27**, 991–1022.

2 R. Pokhrel and G. W. Brudvig, *Phys. Chem. Chem. Phys.*, 2014, **16**, 11812–11821.

3 I. G. McKendry, S. K. Kondaveeti, S. L. Shumlas, D. R. Strongin and M. J. Zdilla, *Dalton Trans.*, 2015, **44**, 12981–12984.

4 M. Wiechen, I. Zaharieva, H. Dau and P. Kurz, *Chem. Sci.*, 2012, **3**, 2330–2339.

5 G. S. Hutchings, Y. Zhang, J. Li, B. T. Yonemoto, X. Zhou, K. Zhu and F. Jiao, *J. Am. Chem. Soc.*, 2015, **137**(12), 4223–4229.

6 J. Wu, G. Wang, J. Du, J. P. Liu, J. Wang and W. Fan, *ChemCatChem*, 2018, **10**, 2551–2557.

7 X. Y. Yu, Y. Feng, B. Guan, X. W. D. Lou and U. Paik, *Energy Environ. Sci.*, 2016, **9**, 1246–1250.

8 Y. Vlamidis, E. Scavetta, M. Gazzano and D. Tonelli, *Electrochim. Acta*, 2016, **188**, 653–660.

9 L. Lv, Z. Yang, K. Chen, C. Wang and Y. Xiong, *Adv. Energy Mater.*, 2019, **9**, 1803358–1803387.

10 R. Renuka and S. Ramamurthy, *J. Power Sources*, 2000, **87**, 144–152.

11 R. C. Remsing, I. G. McKendry, D. R. Strongin, M. L. Klein and M. J. Zdilla, *J. Phys. Chem. Lett.*, 2015, **6**, 4804–4808.

12 A. C. Thenuwara, S. L. Shumlas, N. H. Attanayake, E. B. Cerkez, I. G. McKendry, L. Frazer, E. Borguet, Q. Kang, M. J. Zdilla, J. Sun and D. R. Strongin, *Langmuir*, 2015, **31**, 12807–12813.

13 I. G. McKendry, A. C. Thenuwara, S. L. Shumlas, H. Peng, Y. V. Aulin, P. R. Chinnam, E. Borguet, D. R. Strongin and M. J. Zdilla, *Inorg. Chem.*, 2018, **57**, 557–564.

14 H. Peng, I. G. McKendry, R. Ding, A. C. Thenuwara, Q. Kang, S. L. Shumlas, D. R. Strongin, M. J. Zdilla and J. P. Perdew, *Proc. Natl. Acad. Sci. U. S. A.*, 2017, **114**, 9523–9528.

15 I. G. McKendry, L. J. Mohamad, A. C. Thenuwara, T. Marshall, E. Borguet, D. R. Strongin and M. J. Zdilla, *ACS Energy Lett.*, 2018, **3**, 2280–2285.

16 I. G. McKendry, A. C. Thenuwara, S. L. Shumlas, H. Peng, Y. V. Aulin, P. R. Chinnam, E. Borguet, D. R. Strongin and M. J. Zdilla, *Inorg. Chem.*, 2018, **57**, 557–564.

17 B. Hess, C. Kutzner, D. Van Der Spoel and E. Lindahl, *J. Chem. Theory Comput.*, 2008, **4**, 435–447.

18 R. T. Cygan, J.-J. Liang and A. G. Kalinichev, *J. Phys. Chem. B*, 2004, **108**(4), 1255–1266.

19 R. T. Cygan, J. E. Post, P. J. Heaney and J. D. Kubicki, *Am. Mineral.*, 2012, **97**, 1505–1514.

20 H. Peng, I. G. McKendry, R. Ding, A. C. Thenuwara, Q. Kang, S. L. Shumlas, D. R. Strongin, M. J. Zdilla and J. P. Perdew, *Proc. Natl. Acad. Sci. U. S. A.*, 2017, **114**(36), 9523–9528.

21 S. L. Shumlas, S. Singireddy, A. C. Thenuwara, N. H. Attanayake, R. J. Reeder and D. R. Strongin, *Geochem. Trans.*, 2016, **17**, 5.

22 J. Luo, Q. Zhang, A. Huang, O. Giraldo and S. L. Suib, *Inorg. Chem.*, 1999, **38**, 6106–6113.

23 J. Luo, A. Huang, S. H. Park, S. L. Suib and C.-L. O'Young, *Chem. Mater.*, 1998, **10**, 1561–1568.

24 J. Luo and S. L. Suib, *J. Phys. Chem. B*, 1997, **101**, 10403–10413.

25 C. E. Frey, M. Wiechen and P. Kurz, *Dalton Trans.*, 2014, **43**, 4370–4379.

26 C. C. L. McCrory, S. Jung, J. C. Peters and T. F. Jaramillo, *J. Am. Chem. Soc.*, 2013, **135**, 16977–16987.

27 D. C. Golden, C. C. Chen and J. B. Dixon, *Clays Clay Miner.*, 1987, **35**, 271–280.

28 H. W. Nesbitt and D. Banerjee, *Am. Mineral.*, 1998, **83**, 305–315.

29 Z. Chen, Z. Wang, R. Cai, Y. Xie, J. Yu, X. Long, B. Yang and S. Yang, *Nanoscale*, 2020, **12**, 2472–2478.

30 H. B. Gray and J. R. Winkler, *Biochim. Biophys. Acta, Bioenerg.*, 2010, **1797**, 1563–1572.

31 V. Balzani, A. Credi and M. Venturi, *Chem.–Eur. J.*, 2008, **14**, 26–39.

32 R. C. Remsing and M. L. Klein, *Chem. Phys. Lett.*, 2017, **683**, 478–482.